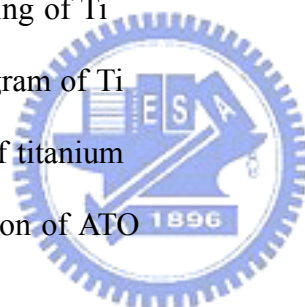


Content

中文摘要	I
Abstract	II
誌謝	III
Content	IV
Tables list	VII
List of figure captions	VIII
Chapter 1 Introduction	1
Chapter 2 Literature Review	3
2.1 Nonlithographic fabrication of nano-technolog	3
2.2 The characteristics and fabrication of nanoscal template	6
2.2.1 Electropolishing of aluminum	6
2.2.2 Anodizing of aluminum	8
2.3 Fabrication of nanowires and its application	14
2.4 The characteristics and fabrication of nanospheres	18
Chapter 3 Experimental Procedures	19
3.1 Electropolishing (EP) of aluminum foil	19
3.2 Anodic Aluminum oxide (AAO)	21
3.3 Fabrication of tin (Sn) nanowires	29

3.4 Methods of nanospheres process	32
Chapter 4 Results and Discussions	35
4.1 Electrochemistry of aluminum	35
4.1.1 Electropolishg of Al	35
4.1.2 Pourbaix diagram of Al	39
4.1.3 Anodization of Al	44
4.2 Comparison of AAO forming by two-step and one-step anodization	45
4.2.1 two-step anodization	45
4.2.2 one-step anodization	51
4.2.3 Self-diffusion of AAO	55
4.2.4 XRD characterization of Al and AAO	58
4.3 AAO growth on the silicon wafer and glass substrate	61
4.4 Defects on the AAO	66
4.5 Sn nanocrystals, whiskers, nanowires, particles and nanospheres forming inside (on) AAO	69
4.5.1 Injection of Sn into AAO forming nanowires	70
4.5.2 Formation of Sn whisker and particles on AAO	93
4.5.3 Formation of Sn nanospheres on AAO	101
4.5.4 Effect of superheating and cooling rate on nanosphere formation	105
4.6 Alloy nanowires and nanoparticles	107
4.6.1 Nanoparticles forming by thermal immersing method	107
4.6.2 Critical radius and free energy of alloy nucleation on	

the AAO	110
4.6.3 Nanoparticle in concave	113
4.6.4 Nanoparticles growth and sintering	115
Chapter 5 Conclusions	122
Chapter 6 Future works	124
References	125
Appendix	132
A.1 Electrochemistry of titanium	132
A.2 Electropolishing of Ti	135
A.3 Pourbaix diagram of Ti	139
A.4 Anodizing of titanium	140
A.5 Decomposition of ATO	148



Tables list

Tab. 2.1 The conditions of anodic to aluminum.	13
Tab. 4.1 The chemical reactions and Nernst's law when aluminum is immersed in aqueous solution.	40
Tab. 4.2 The Nernst's reactions of Al in aqueous solution when Al^{+3} , AlO_2^- ions concentration are 10^{-6} .	41
Tab. A.1 The chemical reactions and Nernst's law when titanium is immersed in aqueous solution.	141



List of figure captions

- Fig. 2.1** The I-V curve of etching, polishing and pitting sections. 7
- Fig. 3.1** Schematic diagram of electropolishing and anodization setup. 20
- Fig. 3.2** The optical microscopy image of aluminum surface after electropolishing. 20
- Fig. 3.3** The first anodization films were removed by mixture of 6 vol% H_3PO_4 and 1.8 wt. % chromic acid (CrO_3) solution, the ordering nanopattern retained on the aluminum surface. The electrolyte of first anodization is by 10 % H_2SO_4 (a), by 3 % $\text{C}_2\text{H}_2\text{O}_4$ (b), and by 2 % H_3PO_4 (c). 23
- Fig. 3.4** The surface morphology of AAO compartment between the first anodization (a), and the second anodization by 3 % oxalic acid electrolyte. 24
- Fig. 3.5** The SEM image of 2nd anodization AAO after pore widening by 6 % phosphoric acid. 24
- Fig. 3.6** The SEM images of AAO bottom view of barrier layer; anodization by 10 vol. % H_2SO_4 electrolyte (a), anodization by 3 vol. % $\text{H}_2\text{C}_2\text{O}_4$ electrolyte (b), and anodization by 2 vol. % H_3PO_4 electrolyte (c). 25
- Fig. 3.7** The flow sheet of AAO process by two steps anodization. 26
- Fig. 3.8** SEM image of AAO forming on the 99.7% purity aluminum foil through 1st anodization, 4 hr at 600°C annealed in the air furnace, and 85 min. 6 vol% H_3PO_4 pore widening at 30°C for 85min. processes. 27
- Fig. 3.9** The flow sheet of AAO process by 99.7 % purity aluminum foil. 28
- Fig. 3.10** The experiment equipment for making metal nanowire. 30

Fig. 3.11 SEM image of Sn melt inside AAO, which formed Sn nanowires: (a) top view, (b) cross-section view.	31
Fig. 3.12 The Sn nanospheres formed by thermo expansion process.	33
Fig. 3.13 The flow sheet of Sn nanospheres fabricated by oil reflowing.	34
Fig. 3.14 Sn spheres forming on the AAO surface by E-beam deposition process.	34
Fig. 3.15 The SEM image of nanospheres on AAO by thermal immersion process.	34
Fig. 4.1 The OM images of mechanical polishing (a), and chemical polishing on pure Al (b).	35
Fig. 4.2 The OM images of EP Al surface without annealing before.	36
Fig. 4.3 The OM images of Al surface after annealing and EP.	36
Fig. 4.4 The OM images of the defects on Al surface after EP; plastic deformation when pre-polishing by Al ₂ O ₃ powder (a), pitting by high voltage (b), and waviness by without stirring.	37
Fig. 4.5 The curve of voltage vs. current density of Al EP.	37
Fig. 4.6 The curve of time vs. current density of Al EP.	37
Fig. 4.7 The OM images of insufficient EP time; 5 sec (a), 10 sec (b), 35 sec (c), 50 sec (d), 500 sec (e), 620 sec (f).	38
Fig. 4.8 The OM images of excessive EP time; 1000 sec (a), 1200 sec (b),	

1400 sec (c). 38

Fig. 4.9 The Pourbaix diagram of Al in electrolytes. 43

Fig. 4.10 Two steps anodization to fabricate AAO using high purity (99.999%) Al foil as substrate in 10% H₂SO₄ solution at 18V, then AAO through pore widening using 5 vol. % H₃PO₄ solution for 0 min (a), 5 min (b), 10 min (c), 15 min (d), 20 min (e), 25 min (f), 30 min (g), 35 min (h), 40 min (i). 46

Fig. 4.11 Two steps anodization to fabricate AAO using high purity (99.999%) Al foil as substrate in 3% CH₂O₄ solution at 40V, then AAO through pore widening using 5% H₃PO₄ solution for 0 min (a), 5 min (b), 10 min (c), 15 min (d), 20 min (e), 25 min (f), 30 min (g), 35 min (h), 40 min (i). 47

Fig. 4.12 SEM images of AAO made from aluminum foil (99.7% purity). The anodized alumina layers were prepared by anodization in 3% oxalic acid at 25°C at 40 V. Bottom view of nanopores with barrier layer before pore widening (a). Non-ordered nanopores appear on top view (b). Top view of AAO with subholes after pore widening (c). The pore structure was destroyed easily without heat treatment, even when the pore widening time was only 50 min. (d). 49

Fig. 4.13 SEM images of AAO bottom views. Barrier layer image (a), barrier layer was etched by 5 wt. % H₃PO₄ solution at 30°C for 30 min (b), for 40 min (c), for 50 min (d), for 60 min (e), and for 70 min (f). 50

Fig. 4.14 SEM images of AAO after heat treatment at 600°C; the pores were sintered, then through pore widening, the pores became ordered. (a) The pores in the AAO were sintered and sub-holes was disappeared after 4 hours heat treatment; (b) the pores of AAO expanded after pore widening for 5 min., (c) the pores of AAO expanded and pores became to ordered after pore widening for 50 min., (d) after pore widening for 70 min. (e) the pores of hexagonally

packed structure on AAO after pore widening for 85 min. (f) AFM image of close-packed ordered nanostructure after self-repair, (g) AAO with a thickness of 9 μm . 51

Fig. 4.15 The top view, cross-section view, and bottom view of AAO, and hexagonal pattern on aluminum surface. (a) Top view of low magnification image of long-range ordered channel array with dimensions of the order of millimeters, (b) bottom view of barrier layer with hexagonally packed structure, (c) cross-sectional view with base of straight tube on the bottom barrier layer, (d) hexagonal pattern on aluminum surface when AAO was removed from substrate. 53

Fig. 4.16 Schematic diagram showing array nanochannel in AAO is through O and Al diffuse into the AAO. 56

Fig. 4.17 Self-diffusion distance of Al_2O_3 with diffusion time at 600°C . 57

Fig. 4.18 On AAO without an Al substrate, the AAO structure was destroyed after heat treatment at 600°C for 4 hours. 57

Fig. 4.19 X-ray diffraction spectrum of AAO before annealing: (a) amorphous AAO, (b) AlPO_4 peaks in the amorphous AAO, after pore widening. 59

Fig. 4.20 X-ray diffraction spectrum of AAO crystallized to γ -phase of Al_2O_3 after annealing. 60

Fig. 4.21 Schematic diagram of self-repair. (a) The holes in AAO were random when Al with a purity of 99.7% was used after anodization, (b) the pores decrease in size towards the center of pore after heat treatment, (c) the pores were expanded by upon pore widening, (d) after long-term pore widening, uniform-sized close-packed ordered nanopore on AAO. 60

Fig. 4.22 Al-Si binary phase diagram 61

- Fig. 4.23** Marco OM image of AAO on the 6 inch Si wafer (a), and 4 inch glass substrate (b). 64
- Fig. 4.24** SEM images of AAO on the 6 inch Si wafer (a), and 4 inch glass substrate (b). 64
- Fig. 4.25** the cross-section SEM images of AAO on Si wafer with barrier layer (a), and without barrier (b). 65
- Fig. 4.26** The transparency of 1 μ m thickness of AAO on the glass substrate. 65
- Fig. 4.27** The SEM images showed the failed AAO when the unsuitable conditions used in anodization; local heat (a), thermo cracking (b), defects (c), pitting (d), grain boundary (e), sub-holds (f), random (f), and breaking (g). 68
- Fig. 4.28** The schematic diagram of metal/ceramic composite of experimental sample. 70
- Fig. 4.29** The schematic diagram of AAO structure (a), to inject melt into the AAO (b), nanowires formed in the AAO (c), removed Al substrate (d), removed barrier layer(e), and removed partial of AAO (f). 71
- Fig. 4.30** The basic Sn bulk material characteristics of micro morphology (a), composition (b), and melting point (c) were detected by OM, XRD, and DSC. 73
- Fig. 4.31** The curve of critical pressure for melt injected in nanochannel; applied pressure increasing with pore size decreasing. 74
- Fig.4.32** Top and bottom view SEM images of filling ratio of Sn inside AAO ($\psi=60\text{nm}$). Top view images of applied pressure 30bar (1750Kg) (a), 35bar (2042Kg) (b), 50bar (2817Kg) (c), and bottom view of applied pressure 50bar (2817Kg) (d) on the Sn melt. 75
- Fig.4.33** Top and bottom view SEM images of filling ratio of Sn inside

AAO ($\psi=15\text{nm}$). Top view images of applied pressure 100 bar (5835 kg) (a), 140.1 bar (8175 kg) (b), 200 bar (11671 kg), and bottom view of applied pressure 200 bar (11671 kg) (d) on the Sn melt. 76

Fig. 4.34 The SEM images of bottom AAO with partial Sn inside; barrier layer retains on AAO (image right side), Empty holes (black), and Sn nanowires inside the holes (white). 77

Fig. 4.35 The SEM images of bottom AAO showed the original (a) AAO with low filling ratio of Sn inside that Sn inside AAO made AAO color from black changed to white. Improved the filling ratios of Sn inside AAO by high temperature (450 °C for 1 hr) drying (b) and high temperature (450 °C) vacuum (10^{-3} torr) treatments; 10 min (c), 15 min (d), 20 min (e), 25 min (f). 78

Fig. 4.36 SEM image of Sn melt inside AAO, which formed Sn nanowires: (a) top view, (b) cross-section view, high magnification of cross-section (top) view, and high magnification of cross-section (bottom) view. 79

Fig. 4.37 DSC curves of the melting point on bulk Sn is 231.7 °C, 60 nm diameter and 15 nm diameter Sn nanowires decrease to 227.1 °C and 224.1 °C. 80

Fig. 4.38 DSC curves of the melting point on bulk Bi is 272.2°C, 60 nm diameter and 15 nm diameter Bi nanowires decrease to 265.3 °C and 256.6 °C. 80

Fig. 4.39 The SEM images of Sn nanowires were collected on the Cu Cu grid after AAO was dissolved in 0.2% NaOH solution; low magnification image (a), and high magnification image (b). 81

Fig. 4.40 TEM micrograph of a randomly selected single nanowire (60 nm). The black circles indicate the areas from which the electron diffraction pattern (ED) was taken. Note that the ED patterns remain the wire length. The zone axis in this case was [021] and the growth direction is [100]. 82

- Fig. 4.41** TEM micrograph of a randomly selected single nanowire (15 nm).
The zone axis in this case was $[\bar{1}11]$ and the growth direction is $[101]$. 83
- Fig. 4.42** XRD patterns of large scale AAO/Sn nanowire composite. 84
- Fig. 4.43** A schematic side view diagram of Sn inside AAO template; with Al substrate and alumina barrier layer (a), without Al substrate and alumina barrier layer (b). 86
- Fig. 4.44** SEM images of sample bottom view; after aluminum substrate was removed, the barrier layer presents (a); furthermore, grain boundary of barrier layer etched by 6% H_3PO_4 solution for 20min at 23°C (b); the solution reacted to the metal Sn for 20min at 23°C (c). 87
- Fig. 4.45** SEM images of AAO ($\psi=180nm$) sample bottom view; barrier layer was removed by 0.2 wt% NaOH at 23°C for 4hr (a), 4hr 30min (b), 5hr (c), 5hr 30min (d). 88
- Fig. 4.46** SEM images of AAO ($\psi=60nm$) sample bottom view; barrier layer was removed by 0.2 wt% NaOH at 23°C for 2hr (a), 2hr 30min (b), 3hr (c), 3hr 30min (d). 90
- Fig. 4.47** SEM images of AAO ($\psi=15nm$) sample bottom view; barrier layer was removed by 0.2 wt% NaOH at 23°C for 30min (a), 40min (b), 50min (c), 60min (d). 91
- Fig. 4.48** SEM image of the order nanopattern retains on the Sn bulk surface. 92
- Fig. 4.49** Sn whiskers and particle growth on 60nm diameter pore of AAO

(with Sn inside) surface, heating up and cooling down by Differential Scanning Calorimetry (DSC); clean surface of AAO at 25°C (a), nanocrystals forming at 220°C (b), whiskers forming at 226°C (c), whiskers agglomeration at 228°C (d), whiskers agglomeration and forming a sphere at 229°C (e), few whiskers connect to sphere at 230°C (f), micro scale sphere forming at 231°C (g), most spheres and few whiskers on the AAO (h), micron and sub-micro spheres on the AAO at 240°C (i). 95

Fig. 4.50 The SEM images of Sn nanowhiskers form on the AAO (a), and the high magnification image (b). 96

Fig. 4.51 The SEM images of Sn nanosphere on the nanowhiskers (a), and the high magnification image (b). 98

Fig. 4.52 The Equilibrium curves of partial oxygen pressure (a) and Gibbs free energy (b) between 150 °C to 300°C in Sn-SnO and Sn-SnO₂ system. 100

Fig. 4.53 SEM image of AAO template with nanoscale roughness of nanopillars and nanopores. 102

Fig. 4.54 The SEM images of rapid solidification of Sn nanospheres on the AAO surface. 102

Fig. 4.55 The SEM image of Sn nanospheres with diameter between 90 and 300 nm. 103

Fig. 4.56 Histogram showing the quantitative size distribution of nanospheres. 103

Fig. 4.57 DSC curves showing the melting points of pure Sn and the Sn nanosphere to be 231.91°C and 227.15°C, respectively. 104

Fig. 4.58 SEM image of Sn nanospheres collected by vibrate in alcohol. 104

Fig. 4.59 TEM image of Sn nanosphere (a), and diffraction pattern with tetragonal crystal structure of [101] zone axis (b). 105

- Fig. 4.60** SEM images showing the AAO surface without any Sn sphere after Sn nanospheres were collected by vibrate, as well as remaining shallow concave wells on the AAO surface. 106
- Fig.4.61** SEM images showing Sn balls cracked under a fast quenching rate (235°C to 0°C). 106
- Fig.4.62** SEM images showing Sn balls sintered together under the high temperature (300°C). 106
- Fig. 4.63** Molten metal became cohered and covered AAO when heat treatment time was insufficient, so that nanoparticles had difficulty forming on AAO. 107
- Fig. 4.64** Schematic diagrams show oxide film existence between melt and AAO, which difficultly in nanoparticle formation on AAO; (a) that macro schematic of oxide film covered on surface of melt, (b) micro schematic of oxide film that prevented melt nucleation on the AAO. 108
- Fig. 4.65** Schematic diagrams showing free oxide on interface of melt-AAO, the nanoparticles formed on AAO; (a) macro schematic of free oxide film on interface of AAO-melt, (b) micro schematic of melt nucleated on AAO. 108
- Fig. 4.66** SEM image showing that melt solidified and nucleated to form nanoparticles on AAO. 109
- Fig. 4.67** Homogeneous nucleation of critical radius and Gibbs free energy of Pb-Bi eutectic are 2.7 nm and 128×10^{-24} joule at 398 K. 109
- Fig. 4.68** Nanoparticle size in a concave was much larger than that on surface of

- Fig. 4.69** Various numbers and sizes of nanoparticles in concaves; (a) diameters of nanoparticles on pore wall of concave were larger than those on surface of AAO, (b) a smooth and shallow indent, numbers and the size of nanoparticles inside were similar to those on surface of AAO, (c) large number of nanoparticles formed in deep and rough concave, (d) small number of large nanoparticles formed in deep concave. 116
- Fig. 4.70** SEM image of nanoparticles subjected to ultrasound. 117
- Fig. 4.71** Schematic diagrams of AAO with pore radius and pore wall width denoted R, W, and L, respectively. 117
- Fig. 4.72** Nanoparticles in smooth concave; (a) diameter and number of nanoparticles in concave were similar to those of nanoparticles on AAO surface, (b) high magnification image, initially isolated nanoparticle, and parts of large sintered ball formed. 118
- Fig. 4.73** SEM image of sintered nanoparticles in deep concave. 119
- Fig. 4.74** Schematic diagram of surface area with various dept of concave. 120
- Fig. 4.75** Latent heat in the concave of AAO increased with depth of semi-cup indent. 120
- Fig. 4.76** SEM and schematic diagrams of nanoparticles nucleated on the corners of AAO and grown on pore of AAO; (a) nanoparticles nucleated on six nooks of AAO, (b) six isolated nanoparticles grew, (c) six nanoparticles assemble to form a large nanoparticle. 121

Fig. A.1 The optical microscopy image of titanium surface after electropolishing.	133
Fig. A.2 The SEM image of ATO.	133
Fig. A.3 The flow sheet of ATO process.	134
Fig. A.4 The electro-polishing curve of titanium.	136
Fig. A.5 The OM images of EP on β phase (a), and α phase Ti surface (b).	136
Fig. A.6. The optical micrographs of electro-polishing progress from 1 to 21 minutes on the titanium surface; (a) original titanium surface; (b)-(h) insufficient polishing, 1 to 13 minutes; (i) suitable polishing, 14 minutes; (j)-(k) excess polishing, 17 to 21 minutes.	138
Fig. A.7 The initially Ti Pourbaix diagram constructed by 22 reactions.	144
Fig. 4.6 The Pourbaix diagram of titanium in electrolytes.	144
Fig. A.9 10% H_2SO_4 + 1.2% HF as the electrolyte, the ordered nanochannel array of ATO formed on the surface of titanium; (a) nanochannel of top view, (b) barrier layer (b) of bottom view.	145
Fig. A.10 The SEM images of ATO forming when anodization time at 10 sec (a), 20 sec (b), 30 sec (c), 40 sec (d), 50 sec (e), 60 sec (f), 70 sec (g), 80 sec (h), and 90 sec (i).	146
Fig. A.11 DTA curves of porous and dense ATO; an exothermic peak was detected at 581°C for porous ATO, but no any peak be detected relatively dense ATO until 670 °C.	150